

Physical realization of a quantum spin liquid based on a complex frustration mechanism

Christian Balz^{1,2*}, Bella Lake^{1,2}, Johannes Reuther^{1,3}, Hubertus Luetkens⁴, Rico Schönnemann⁵, Thomas Herrmannsdörfer⁵, Yogesh Singh⁶, A. T. M. Nazmul Islam¹, Elisa M. Wheeler⁷, Jose A. Rodriguez-Rivera^{8,9}, Tatiana Guidi¹⁰, Giovanna G. Simeoni¹¹, Chris Baines⁴ and Hanjo Ryll¹

Unlike conventional magnets where the magnetic moments are partially or completely static in the ground state, in a quantum spin liquid they remain in collective motion down to the lowest temperatures. The importance of this state is that it is coherent and highly entangled without breaking local symmetries. In the case of magnets with isotropic interactions, spin-liquid behaviour is sought in simple lattices with antiferromagnetic interactions that favour antiparallel alignments of the magnetic moments and are incompatible with the lattice geometries. Despite an extensive search, experimental realizations remain very few. Here we investigate the novel, unexplored magnet $\text{Ca}_{10}\text{Cr}_7\text{O}_{28}$, which has a complex Hamiltonian consisting of several different isotropic interactions and where the ferromagnetic couplings are stronger than the antiferromagnetic ones. We show both experimentally and theoretically that it displays all the features expected of a quantum spin liquid. Thus spin-liquid behaviour in isotropic magnets is not restricted to the simple idealized models currently investigated, but can be compatible with complex structures and ferromagnetic interactions.

A spin liquid is built from a macroscopic lattice of interacting magnetic ions whose ground state has no static magnetism, instead the magnetic moments fluctuate coherently down to the lowest temperatures without breaking local symmetries^{1,2}. It contrasts with the magnetically long-range ordered ground states observed in conventional magnets. Spin-liquid behaviour can arise when competition (known as frustration) between interactions and/or anisotropies suppresses long-range magnetic order. The emergent states reveal new types of topological order which manifest in the existence of excitations with fractional quantum numbers.

Several important spin liquids arise from anisotropic interactions that are incompatible with the lattice geometries; such as spin ice, where ferromagnetic interactions compete with local anisotropies destroying long-range order and giving rise to free monopole excitations^{3,4}. Another example is the Kitaev spin liquid, where competition between highly directional interactions suppresses order and produces Majorana fermion excitations^{5,6}. In the absence of anisotropy, the possibilities for competition are reduced. While both ferromagnetic and antiferromagnetic interactions are capable of frustration if they are anisotropic, it is widely believed that isotropic interactions (known as Heisenberg interactions) must be predominantly antiferromagnetic to generate frustration. This is because, for ferromagnetic Heisenberg interactions, the spins can rotate and align parallel to each other on any lattice, satisfying all the interactions simultaneously and giving rise to ferromagnetic long-range order.

Specific lattices are required for the spin-liquid state in Heisenberg antiferromagnets. Geometrical frustration is possible when the magnetic ions are arranged on triangular or tetrahedral units, here the antiferromagnetic coupling favours antiparallel spin alignment between nearest-neighbour spins, which can never be satisfied on all magnetic bonds. This typically leads to highly degenerate ground states and the tendency for static long-range order to be reduced. This tendency can be further suppressed in quantum systems where the magnetic ions have quantum spin number $S = 1/2$; here the Heisenberg uncertainty principle produces zero-point motion that is comparable to the size of the spin and which persists down to $T = 0$ K.

Theoretical work on quantum spin liquids with isotropic antiferromagnetic interactions has resulted in a number of models. The most promising two-dimensional quantum spin liquid is the kagome lattice consisting of corner-sharing triangles of antiferromagnetically coupled spin-1/2 ions^{7–11}. Experimental realizations are in contrast much more challenging because real materials usually have additional terms in their Hamiltonians, such as further-neighbour interactions which can lift the degeneracy, destroying the spin-liquid ground state¹². Among the many proposed physical realizations of the kagome lattice, the best candidate is the mineral Herbertsmithite, which has recently been verified as a quantum spin liquid^{13,14}. Herbertsmithite has no long-range order down to the lowest temperatures, and its excitations are spinons which have fractional quantum spin number $S = 1/2$, and

¹Helmholtz-Zentrum Berlin für Materialien und Energie, 14109 Berlin, Germany. ²Institut für Festkörperphysik, Technische Universität Berlin, 10623 Berlin, Germany. ³Dahlem Center for Complex Quantum Systems and Fachbereich Physik, Freie Universität Berlin, 14195 Berlin, Germany. ⁴Laboratory for Muon-Spin Spectroscopy, Paul Scherrer Institut, 5232 Villigen, Switzerland. ⁵Hochfeld-Magnetlabor Dresden (HLD-EMFL), Helmholtz-Zentrum Dresden-Rossendorf, 01314 Dresden, Germany. ⁶Indian Institute of Science Education and Research (IISER) Mohali, Knowledge City, Sector 81, Mohali 140306, India. ⁷Institut Laue-Langevin, 38042 Grenoble, France. ⁸NIST Center for Neutron Research, National Institute of Standards and Technology, 20899 Gaithersburg, USA. ⁹Department of Materials Science, University of Maryland, College Park, 20742 Maryland, USA. ¹⁰ISIS Facility, STFC Rutherford Appleton Laboratory, Oxfordshire OX11 0QX, UK. ¹¹Heinz Maier-Leibnitz Zentrum, Technische Universität München, 85748 Garching, Germany. *e-mail: christian.balz@helmholtz-berlin.de

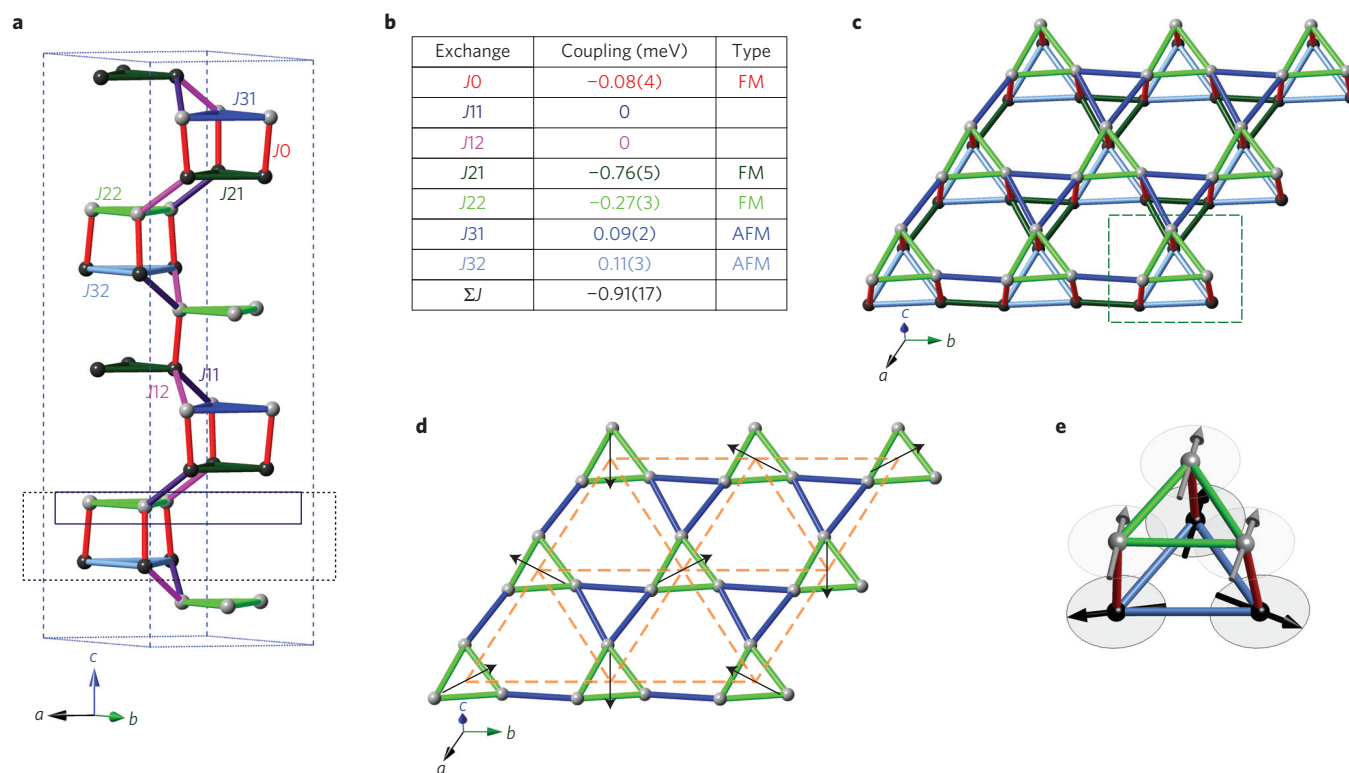


Figure 1 | Structure and Hamiltonian. **a**, Crystallographic unit cell of $\text{Ca}_{10}\text{Cr}_7\text{O}_{28}$ showing only the magnetic Cr^{5+} ions, which are represented by the black and grey spheres (see Supplementary Methods for details of the crystal structure determination). The seven nearest-neighbour couplings between Cr^{5+} ions are indicated by the coloured lines. **b**, Values of isotropic (Heisenberg) exchange interactions corresponding to the magnetic couplings in **a**, FM means ferromagnetic and AFM means antiferromagnetic (see Supplementary Methods for details on how the Hamiltonian and its error bars were deduced). **c**, The crystal structure consists of distorted kagome bilayers of Cr^{5+} ions lying in the ab plane. The two layers which form the bilayer both consist of two different corner-sharing equilateral triangles, which alternate in the ab plane. The green triangles are ferromagnetically coupled and the blue triangles are antiferromagnetically coupled. It should further be noted that the two layers are inequivalent and have interactions of different sizes. These two layers are coupled together into a bilayer via the ferromagnetic interaction J_0 (red bond) that connects the ferromagnetic triangles of one layer directly to the antiferromagnetic triangles in the second layer, and vice versa. The bilayers were found to be magnetically isolated from each other ($J_{11} = J_{12} = 0$) and are stacked along the c axis, as shown in **a**. **d**, Kagome single-layer magnetic model. The dashed orange triangles and the black arrows give the 120° order of the effective $S=3/2$ triangular lattice. **e**, Snapshot of the fluctuating ground state spin arrangement for one bi-triangle consisting of a ferromagnetic upper triangle coupled to an antiferromagnetic lower triangle. This corresponds to the frustrated unit in $\text{Ca}_{10}\text{Cr}_7\text{O}_{28}$.

are very different from the $S=1$ spin waves or magnon excitations that characterize conventional magnets.

Here we introduce the Heisenberg quantum magnet $\text{Ca}_{10}\text{Cr}_7\text{O}_{28}$. Its crystal structure consists of distorted kagome bilayers of Cr^{5+} ions which have spin-1/2 moments (Fig. 1a)¹⁵ (also Balz, manuscript in preparation). A single bilayer is shown in Fig. 1c, where the interactions are represented by the coloured lines. The two kagome planes that form the bilayer are different, and consist of inequivalent alternating equilateral triangles. The Hamiltonian consists of five different isotropic interactions, which are both ferromagnetic and antiferromagnetic, but where the ferromagnetic interactions are significantly stronger. This coupling scheme is much more complex than any that has been investigated previously, and would never be proposed for spin-liquid behaviour, due to the dominant ferromagnetic interactions. Here we show that the magnetic properties of $\text{Ca}_{10}\text{Cr}_7\text{O}_{28}$ are consistent with a quantum spin liquid, by using a range of experimental techniques as well as functional renormalization group calculations. Thus, spin-liquid behaviour in isotropic magnets is not restricted to the simple idealized models currently being investigated, but can be compatible with complex structures and ferromagnetic interactions. Furthermore, high-quality single crystals can be made with relative ease, and the complex magnetic Hamiltonian opens up opportunities for manipulating the spin-liquid state in $\text{Ca}_{10}\text{Cr}_7\text{O}_{28}$.

Among the key features of a quantum spin liquid is the absence of static magnetism in the ground state. A second-order phase transition to long-range magnetic order is revealed by a sharp lambda-shaped anomaly in the temperature-dependent specific heat. The specific heat of $\text{Ca}_{10}\text{Cr}_7\text{O}_{28}$ is shown in Fig. 2a; no lambda anomaly is evident, proving that no phase transition occurs down to 0.3 K. The magnetic specific heat, however, shows a broad peak at $T^* \approx 3.1$ K, indicating the onset of coherent quantum fluctuations, and a weak kink at $T^+ = 0.46$ K suggests a possible crossover at this temperature. The reduced magnetic specific heat $C_p(T)/T$ can be integrated to extract the entropy, and reveals that 90% of the total magnetic entropy (for spin-1/2 ions) is recovered over the temperature range 0.3–23.3 K (Fig. 2a). Thus, if a transition occurs below 0.3 K it can release at most 10% of the entropy, implying that the ordered moment would be highly suppressed.

A common reason for the absence of long-range magnetic order is that the ground state is a valence bond solid. Here all the $S=1/2$ magnetic ions form pairs or valence bonds where the two spins have antiparallel alignment and form singlets (total spin zero). The singlet arrangement is fixed throughout the lattice, and the excitations are gapped magnons ($S=1$) corresponding to promoting the singlets into triplets. It should be noted that, although the valence bond solid has no long-range magnetic order, it is not a spin liquid because the fixed spin pairing breaks local symmetry¹⁶. The characteristic

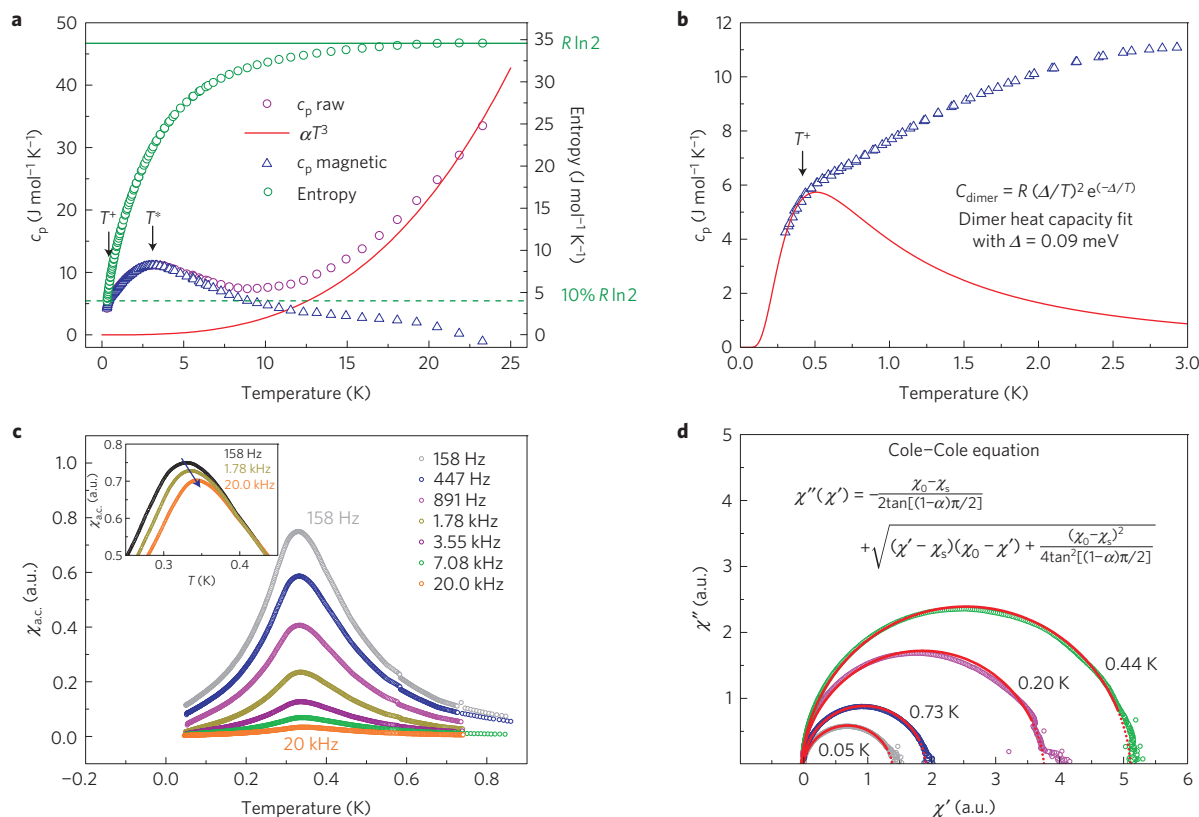


Figure 2 | Specific heat and a.c. susceptibility. **a**, Low-temperature heat capacity before (purple circles) and after (blue triangles) subtraction of a Debye-like phonon contribution $C_p = \alpha T^3$ (red line). The magnetic entropy $S = \int (C_p/T) dT$ (green circles), where the integration is from 0.3 to 23.3 K, is plotted on the right axis while the total possible entropy ($R \ln 2$ for spin-1/2) is indicated by the green line. **b**, Magnetic heat capacity below 3 K (blue triangles). The expression for the specific heat of a gapped dimer magnet as shown in the figure is fitted to the data below 0.46 K (red line) and allows the upper limit of a possible energy gap to be estimated as $\Delta = 0.09$ meV. **c**, Temperature dependence of the magnitude of the a.c. susceptibility $\chi_{ac} = \sqrt{\chi'^2 + \chi''^2}$ for a range of frequencies ω measured with $\mu_0 H_{dc} = 0$ T and $\mu_0 H_{ac} = 30$ μ T. The scaled frequency-dependent shift of the maximum is shown in the inset. This shift is fitted to $\phi = (1/T_f)(\Delta T_f / \Delta \log_{10} \omega)$, where T_f is the temperature corresponding to the observed maximum for the lowest frequency and yields a Mydosh parameter of $\phi = 0.022$. **d**, Cole-Cole plot (χ'' versus χ') for different temperatures¹⁹. Each temperature is fitted individually to the Cole-Cole equation given in the figure, where data in the frequency range 100–20,000 Hz was used. The signal below 100 Hz is too weak to obtain reliable data. The Cole-Cole parameter α yields 0.11, 0.06, 0.05 and 0.05 for 50 mK, 200 mK, 440 mK and 730 mK, respectively.

energy gap of this state is easily observed in the specific heat as an exponential increase at low temperatures. To give an upper limit for the gap size, the data below 0.46 K were fitted and show that if a gap exists it must be smaller than 0.09 meV (Fig. 2b), thus making a valence bond solid state unlikely.

Another explanation for the absence of a magnetic phase transition is that the ground state is a spin glass. Here the spins are static, but have no long-range order, instead they become locked into short-range ordered configurations below the spin freezing temperature. The freezing temperature is not a true transition and has no distinct signature in specific heat; however, a spin glass can be identified in the a.c. susceptibility by its broad distribution of relaxation times¹⁷. The a.c. susceptibility measures the in-phase (χ'), and out-of-phase (χ'') components of the magnetic response of the sample to an alternating magnetic field. By changing the frequency it is possible to probe the relaxation times present in the sample. The amplitude of the a.c. susceptibility of $\text{Ca}_{10}\text{Cr}_7\text{O}_{28}$ as a function of temperature down to 0.05 K for a range of frequencies is shown in Fig. 2c. A broad maximum is observed at 0.33 K, close to where the weak kink is observed in the heat capacity. This peak shifts by 0.015 K over the entire frequency range (Mydosh parameter $\phi = 0.022$); this shift is typical either for an insulating spin glass or the presence of slow dynamics¹⁸.

However, spin-glass behaviour is ruled out by the Cole-Cole plot, where χ'' is plotted against χ' as the frequency is varied

for different temperatures (Fig. 2d). A perfect semicircle indicates a single relaxation time, whereas a flattened semicircle reveals a distribution of relaxation times¹⁹. The size of the relaxation time distribution is quantified by the Cole-Cole parameter α , which takes values from 0 to 1. For $\text{Ca}_{10}\text{Cr}_7\text{O}_{28}$, α lies in the range 0.05–0.11, consistent with a single relaxation time, while for a typical spin glass it is greater than 0.75¹⁷.

Muon spin relaxation (μ SR) is an extremely sensitive local probe of short- and long-range magnetic order, able to detect tiny magnetic moments and distinguish between static and dynamic behaviour. Spin-polarized muons are implanted in the sample at a specific interstitial lattice site and undergo Larmor precession due to the local magnetic field at this site. The muon spin polarization as a function of time, $P(t)$, probes the magnetism in the sample. In the presence of long-range magnetic order, the magnetic field experienced by the muons is static and $P(t)$ oscillates due to the Larmor precession of the muon spin. In contrast, dynamical fields which fluctuate during the muon lifetime rapidly relax $P(t)$, and no oscillations are observed²⁰. The time-dependent muon spin polarization of $\text{Ca}_{10}\text{Cr}_7\text{O}_{28}$ displayed in Fig. 3a exhibits an increasing relaxation (damping) as temperature is decreased; however, no oscillations are observed down to 0.019 K. While the absence of oscillations usually indicates the absence of long-range static magnetic order²⁰, the increasing relaxation could be due to static magnetism, with a broad distribution of local fields at the muon

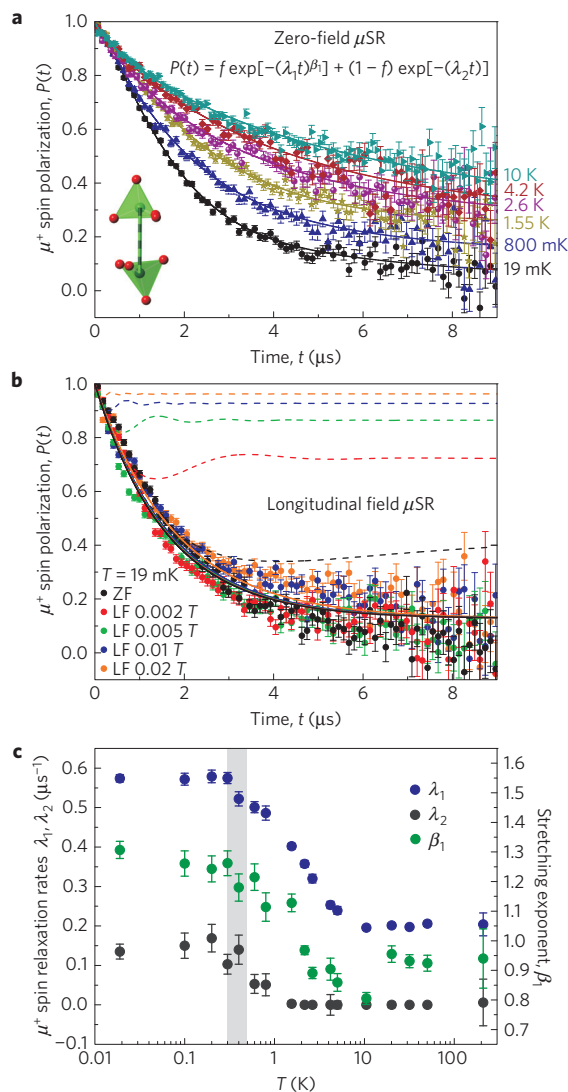


Figure 3 | μ SR data. **a**, Time-dependent muon spin polarization $P(t)$ of $\text{Ca}_{10}\text{Cr}_7\text{O}_{28}$ at selected temperatures measured in zero field. Solid lines are fits to the data using the equation shown in the figure. This equation consists of two relaxation processes, where f is the fraction of the fast relaxation process, λ_1 and λ_2 are the fast and slow relaxation rates, respectively, and β_1 is the stretching exponent of the fast relaxation rate. The two relaxation processes were found to have the weighting 3:1. This is consistent with the ratio of the two muon sites expected from the crystal structure. The inset shows the nearest-neighbour CrO_4 tetrahedra; the muons can implant close to either the three in-plane oxygen (giving the fast relaxation) or the one apical oxygen (giving the slow relaxation). **b**, Data collected in a longitudinal magnetic field at 19 mK. The zero-field data is fitted to the theoretical Kubo-Toyabe functions for both static (dashed black line) and dynamic (solid black line) relaxation⁴⁶. Using the fitted parameters, the static (dashed lines) and dynamic (solid lines) relaxation is then simulated for various longitudinal fields. Comparison to the data clearly gives much better agreement with the predictions for a dynamical ground state. The colour code of the simulations corresponds to the colour code of the data. **c**, Temperature dependence of λ_1 , λ_2 and β_1 , as given in the equation shown in **a**. The shaded region from 0.3 to 0.5 K where the relaxation becomes constant coincides with the temperature where the a.c. susceptibility goes through a maximum and the specific heat shows a kink. The broad peak at 3.1 K in the specific heat corresponds to the temperature where the relaxation rates start to increase. The error bars in **a** and **b** represent one standard deviation, the error bars in **c** are the standard errors of the respective fit parameter.

site preventing coherent precession. This is observed in spin glasses and magnetic systems with many structurally different interstitial muon sites.

The presence of static magnetism can be unequivocally ruled out by μ SR measurements in a longitudinal magnetic field. In the presence of static magnetism, a field applied parallel to the initial muon spin direction would decouple $P(t)$ from the internal fields. At external fields about ten times the internal field, $P(t)$ would become constant as a function of time. However, in a dynamic magnetic system this decoupling is not possible for small fields, and $P(t)$ is essentially unaffected by the external field²⁰. Therefore, the μ SR data presented in Fig. 3b, which were measured in several longitudinal fields at 0.019 K, clearly reveal that the magnetic ground state is entirely dynamic.

To learn more about the dynamical behaviour of $\text{Ca}_{10}\text{Cr}_7\text{O}_{28}$, the zero-field spectra were fitted to extract the relaxation rate as a function of temperature. The fitted expression is shown in Fig. 3a; two relaxation rates were assumed because two muon sites are expected from the crystal structure. The temperature dependences of the relaxation rates, λ_i , are plotted in Fig. 3c; they increase on cooling below 3 K and then become constant below ~ 0.3 – 0.5 K. This result shows that $\text{Ca}_{10}\text{Cr}_7\text{O}_{28}$ enters a low-temperature regime where the dynamics are persistent and independent of temperature. The temperature dependence of the relaxation rate is similar to that of the well-studied quantum spin liquid Herbertsmithite²¹, as well as other systems proposed as spin liquids^{22,23}.

Together, heat capacity, a.c. susceptibility and μ SR reveal the complete absence of static magnetism in $\text{Ca}_{10}\text{Cr}_7\text{O}_{28}$. Both long-range magnetic order and spin-glass freezing are absent down to 0.019 K. Furthermore, they exclude a spin gap greater than 0.09 meV, thus making a valence bond solid scenario unlikely. Most importantly, μ SR and a.c. susceptibility show that the spins are fluctuating coherently down to the lowest temperatures, and that the fluctuation rate becomes constant below 0.3 K, revealing a ground state characterized by persistent slow dynamics, as would be expected for a quantum spin liquid.

To explore the dynamics of $\text{Ca}_{10}\text{Cr}_7\text{O}_{28}$ in more detail we used inelastic neutron scattering. The neutron scattering cross-section is directly proportional to the dynamical structure factor $S(Q, \omega)$, which is the Fourier transform in space and time of the spin-spin correlation function and allows the magnetic excitations to be mapped out as a function of energy and wavevector transfer²⁴. Figure 4a shows the powder spectrum, in which the excitations appear gapless and form two distinct bands with energy ranges 0.0–0.6 meV and 0.7–1.5 meV. No magnetic scattering is found above 1.6 meV. Measurements on a single crystal were also performed. Figure 4b shows the excitations as a function of energy and wavevector within the plane of the kagome bilayers. While confirming the presence of two bands it is clear that the excitations are dispersionless and much broader than the instrumental resolution of 0.025 meV. Figure 4c–h shows the in-plane excitations at various fixed energy transfers. The magnetic scattering is broad and diffuse at all energies. The scattering in the lower band (Fig. 4c,e) forms diffuse ring-like features very different from the diffuse blocks of scattering observed in the upper band (Fig. 4f–h); however, within each band the excitations evolve only gradually with energy. Figure 4d shows the spectrum perpendicular to the kagome bilayers at 0.25 meV, the signal does not disperse along the out-of-plane direction ($[0,0,l]$), proving that the bilayers are magnetically isolated from each other and the magnetism is essentially two-dimensional (further evidence for the two-dimensionality is provided by data taken at high magnetic fields, as shown in the Supplementary Methods).

The presence of broad, diffuse excitations contrasts strongly with the sharp and dispersive spin-wave modes typical of conventional magnets that have long-range magnetically ordered ground states.

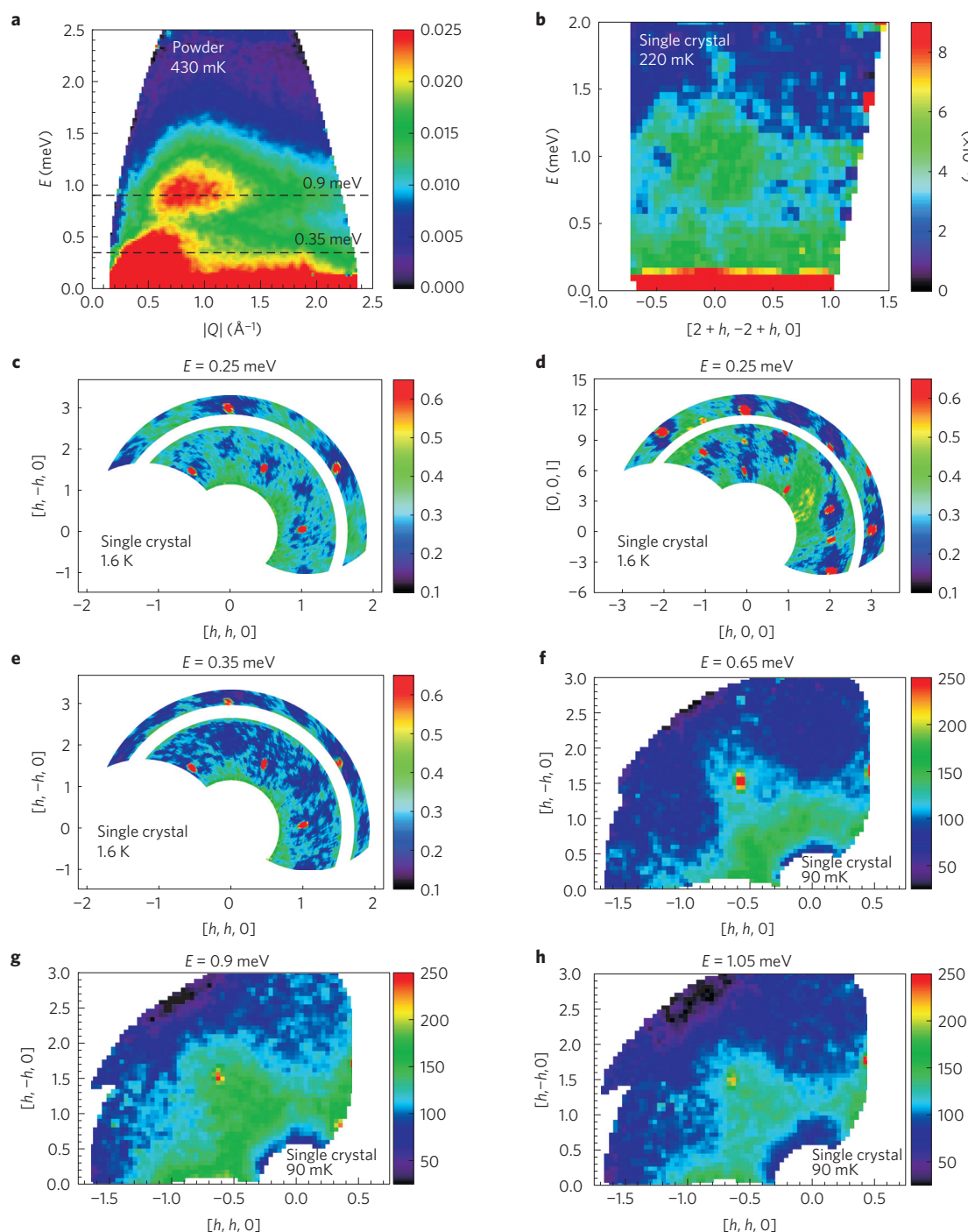


Figure 4 | Inelastic neutron scattering data measured in zero applied magnetic field. a, Powder data measured on TOFTOF at $T = 430$ mK using an incident energy of $E_i = 3.27$ meV. The data are plotted as a function of energy and wavevector transfer. The energy transfers of the constant energy slices shown in **e** and **g** are indicated by the horizontal dashed lines. Data collected using higher incident energies reveal the complete absence of a magnetic signal above 1.6 meV. **b**, Single-crystal data measured on OSIRIS at $T = 220$ mK. The data are plotted as a function of energy and wavevector transfer parallel to $[2 + h, -2 + h, 0]$ and integrated over the perpendicular wavevector range $1.9 < [k, -k, 0] < 2.1$. There are two bands of excitations at 0–0.6 meV and 0.7–1.5 meV, the low-energy signal at 0–0.2 meV is dominated by nuclear and incoherent scattering. Constant-energy slices were measured at 1.6 K on a single crystal using the IN14 spectrometer. **c–e**, Single-crystal data are shown in the plane of the kagome bilayer ($(hk0)$ plane) at 0.25 meV (**c**) and 0.35 meV (**e**), and perpendicular to the bilayers ($(h, 0, l)$ plane) at 0.25 meV (**d**). These energies correspond to the lower excitation band. **f–h**, Single-crystal data were also collected in the upper excitation band in the $(hk0)$ plane at $T = 90$ mK using the MACS II spectrometer at energy transfers of 0.65 (**f**), 0.9 (**g**) and 1.05 meV (**h**). The red high-intensity points in **c–h** are phonons dispersing from Bragg peaks.

Diffuse excitations are also incompatible with a valence bond solid, where a fixed arrangement of singlets in the ground state gives rise to sharp gapped modes. In addition, a valence bond glass scenario seems very unlikely. Here the dimer arrangement is also fixed,

although it is disordered. Its spectrum consists of a small percentage of quasi-free spins which form states below a broadened dimer gap^{25,26}. However, the subgap signal is weak, leading to reduced intensity at low energies, in contrast to observations for $\text{Ca}_{10}\text{Cr}_7\text{O}_{28}$.

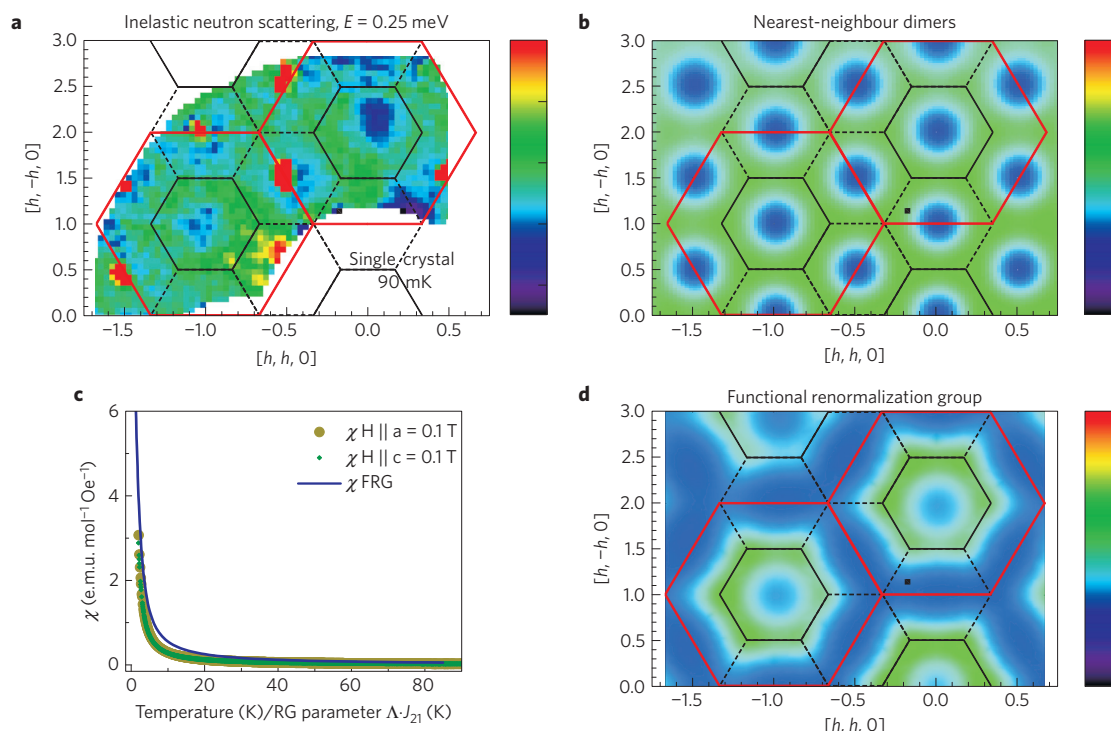


Figure 5 | Inelastic neutron scattering data measured in zero applied magnetic field compared to theory. **a**, Inelastic neutron scattering intensity in the plane of the kagome bilayers ($hk0$) plane) measured on MACS II at $E = 0.25$ meV, $T = 90$ mK. The black (red) lines are the boundaries of the first (fourth) Brillouin zone. The red high-intensity points are phonons dispersing from Bragg peaks. **b**, Equal-time structure factor for dimers randomly arranged on a triangular lattice using the method described in ref. 13. The lattice spacing is assumed to be twice the average in-plane nearest-neighbour Cr^{5+} – Cr^{5+} distance, corresponding to the effective S -3/2 triangular lattice proposed for $\text{Ca}_{10}\text{Cr}_7\text{O}_{28}$ (dashed orange lines in Fig. 1d). The calculated intensity was multiplied by the magnetic form factor of Cr^{5+} . This model captures the ring-like intensity modulation of the data. **c**, d.c. susceptibility measured with a magnetic field of $H = 0.1$ T applied parallel to the a and c axes, plotted alongside the PFFRG susceptibility at $Q = 0$ calculated for the Hamiltonian of $\text{Ca}_{10}\text{Cr}_7\text{O}_{28}$ (see Supplementary Methods for further details). **d**, Q -space-resolved susceptibility at $E = 0$ meV and $T = 0$ K calculated via PFFRG. The signal is corrected for the distortion of the lattice from ideal kagome symmetry, as well as for the magnetic form factor of Cr^{5+} . Diffuse hexagonal-shaped scattering is obtained, with broad maxima at the corners of the first Brillouin zone.

On the other hand, the excitations of a quantum spin liquid are expected to be spinons which have a spin quantum number of $S = 1/2$. Spinons are well established in the one-dimensional, spin-1/2, Heisenberg antiferromagnet^{27–32}, but their existence in higher dimensions is more controversial. They are believed to be the fundamental excitations of the resonating valence bond state, which is one of the main conceptual models for a quantum spin liquid¹. Here, as for the valence bond solid, all the spin-1/2 magnetic ions pair into singlets. However, in contrast to the fixed spin pairing of the valence bond solid, which breaks local symmetry¹⁶, pairing configurations in the resonating valence bond state fluctuate over a number of different arrangements, with no preference for any particular one, leading to long-range entanglement³³. Excitations can be created by exciting a valence bond from its singlet to its triplet state. Unlike for a conventional magnet, this magnon ($S = 1$) excitation can dissociate (or fractionalize) into two spinons ($S = 1/2$), which are able to move apart without costing additional energy via a simple rearrangement of the fluctuating valence bonds already superimposed in the ground state^{34–37}. In inelastic neutron scattering, spinons are observed as broad continuous features rather than sharp modes. This is a consequence of the neutron scattering selection rule $\Delta S = 0, \pm 1$, which prevents a single spinon from being created; instead, they must be created in multiple pairs to conserve spin angular momentum.

A spinon continuum was recently observed in Herbertsmithite, which is the best realization of the Heisenberg, spin-1/2, kagome antiferromagnet. Dispersionless diffuse excitations were found¹³. The spectrum has similarities to $\text{Ca}_{10}\text{Cr}_7\text{O}_{28}$, as both show broad,

hexagonal rings at low energies. However, there are several differences: first, $\text{Ca}_{10}\text{Cr}_7\text{O}_{28}$ has two bands of excitations rather than the single band observed in Herbertsmithite; this might simply be a consequence of its bilayer structure and more complex Hamiltonian. Second, and more significantly, although both compounds are based on kagome layers, the sizes of their hexagonal rings are different. While Herbertsmithite shows a strong signal along the fourth Brillouin zone boundary (red lines in Fig. 5a), the low-energy band of $\text{Ca}_{10}\text{Cr}_7\text{O}_{28}$ exhibits smaller hexagonal rings at the first Brillouin zone boundary (solid black lines). Additional weaker features are observed along the dashed lines.

Dominant scattering at the first Brillouin zone boundary suggests significant antiferromagnetic correlations, with a distance that is twice the first-neighbour in-plane Cr^{5+} – Cr^{5+} distance. The data at 0.25 meV were compared to the equal-time structure factor for uncorrelated valence bonds on a triangular lattice with lattice parameter twice the first-neighbour distance using the method described in ref. 13 (Fig. 5b). Even though this model neglects correlations within the small Kagome triangles, it captures the observed intensity modulation, verifying the importance of this length scale.

To make further progress it is clear that the Hamiltonian of $\text{Ca}_{10}\text{Cr}_7\text{O}_{28}$ needs to be determined. This is achieved by performing inelastic neutron scattering measurements in an external magnetic field strong enough to force all the spins to align parallel to the field direction. As a result, quantum fluctuations are suppressed and the excitations are spin waves. These can be measured and fitted to spin-wave theory to extract the exchange interactions using the method

described in refs 38,39 (see Supplementary Methods). The model Hamiltonian is

$$\mathcal{H} = \sum_{ij} J_{ij} \mathbf{S}_i \cdot \mathbf{S}_j \quad (1)$$

where J_{ij} are the first seven neighbour exchange interactions shown in Fig. 1a. Heisenberg interactions are assumed. This is justified because, as a light transition metal with only one electron in the 3d shell, the orbital moment of Cr^{5+} is quenched by the strong and distorted tetrahedral crystal field due to the surrounding O^{2-} ions. The d.c. susceptibility confirms that the interactions are isotropic, since no difference between the in-plane and out-of-plane field directions was observed (Fig. 5c). A total of 40 constant-wavevector cuts along two dispersion directions ($[h, -h, 0]$ and $[2+h, -2+h, 0]$) were fitted using the SpinW Matlab library⁴⁰. Slices through the data along other dispersion directions were performed and compared to the corresponding simulations as a further check of accuracy. The values of the extracted exchange interactions are given in Fig. 1b. Both layers of the bilayer consist of alternating equilateral triangles where the Cr^{5+} ions are respectively coupled ferromagnetically (green bonds) and antiferromagnetically (blue bonds); however, the sizes of the interaction in the two layers are different. These layers are coupled together via a weak ferromagnetic interaction (red bonds) connecting the ferromagnetic triangles in one layer directly to the antiferromagnetic triangles in the second layer, and vice versa. The ferromagnetic interactions are significantly stronger than the antiferromagnetic ones, in contradiction to conventional understanding that predominantly antiferromagnetic interactions are necessary to achieve frustration in Heisenberg magnets.

To gain further insight into the properties of this compound we performed pseudofermion functional renormalization group (PFFRG) calculations^{41–43}. This technique can compute the static susceptibility and accurately determine whether a specific Hamiltonian develops static long-range magnetic order. PFFRG calculations performed using the Hamiltonian of $\text{Ca}_{10}\text{Cr}_7\text{O}_{28}$ clearly show the absence of static magnetism, verifying the experimental results. The calculated susceptibility at $Q=0$ is shown in Fig. 5c. As for the measured d.c. susceptibility, it increases smoothly with decreasing temperature. No sharp features are observed down to $T=0$ K, confirming the absence of any phase transition.

Figure 5d shows the PFFRG susceptibility as a function of wavevector within the kagome bilayer at $E=0$ meV and $T=0$ K and reproduces the diffuse hexagonal rings observed in the data at 0.25 meV (Fig. 5a). While the theoretical correlations are clearly short range, their intensity varies, being strongest near the vertices of the hexagon. This is where Bragg peaks would be observed in the case of 120° Néel order on a triangular lattice antiferromagnet with a lattice constant twice the first-neighbour in-plane Cr^{5+} – Cr^{5+} distance, confirming the presence of dominant antiferromagnetic correlations on this length scale in $\text{Ca}_{10}\text{Cr}_7\text{O}_{28}$. Additional scattering observed along the dashed lines in the data is stronger than that calculated in the ground state by PFFRG, possibly because the neutron data is collected at a finite energy (the high incoherent background at $E=0$ meV prevented measurement of the static susceptibility).

While the complex structure of our Hamiltonian for $\text{Ca}_{10}\text{Cr}_7\text{O}_{28}$ might suggest that a specific set of parameters is necessary to suppress long-range magnetic order, this is actually not the case. Additional PFFRG calculations show that the spin-liquid regime is remarkably robust to changes in the values of the exchange interactions. As described in the Supplementary Methods, long-range order is absent even when the exchange constants were varied with respect to each other by up to 50%. Interestingly, the asymmetry of the couplings in the two layers was found to play an important role in the frustration. Calculations where the two layers are made

the same ($J_{21}=J_{22}$ and $J_{31}=J_{32}$) showed tendencies towards magnetic order.

Taken together, the experimental and theoretical results described here provide strong evidence that $\text{Ca}_{10}\text{Cr}_7\text{O}_{28}$ is a quantum spin liquid characterized by slow dynamical fluctuations in the ground state, absence of static magnetism, and excitations that are diffuse and reminiscent of spinon continua. The remaining question is why the Hamiltonian of $\text{Ca}_{10}\text{Cr}_7\text{O}_{28}$ supports spin-liquid behaviour. This Hamiltonian has never been studied before and is much more complex than the models currently proposed for resonating valence bond states. Furthermore, with significantly stronger ferromagnetic interactions than antiferromagnetic interactions, as well as no anisotropy, the source of frustration is not obvious. The clue comes from the inelastic neutron scattering data at low energy transfers and the PFFRG calculations, which show that $\text{Ca}_{10}\text{Cr}_7\text{O}_{28}$ has short-range correlations at wavevectors expected for a triangular antiferromagnet with lattice parameter twice that of the first-neighbour in-plane Cr^{5+} – Cr^{5+} distance.

Within each of the kagome layers that form the bilayer, the dominant ferromagnetic triangles couple the three spin-1/2 Cr^{5+} ions into effective spin-3/2 objects. The weaker antiferromagnetic interactions then couple these spin-3/2 objects into an effective triangular lattice (dashed orange lines in Fig. 1d). The ground state of a spin-3/2 triangular Heisenberg antiferromagnet is well established to have static long-range magnetic order where nearest-neighbour spins point at 120° with respect to each other, while the excitations can be approximated by renormalized spin waves^{44,45}. The additional source of frustration which prevents $\text{Ca}_{10}\text{Cr}_7\text{O}_{28}$ from developing long-range magnetic order and causes the spin waves to fractionalize into spinons must therefore arise from the ferromagnetic intralayer coupling J_0 which couples the ferromagnetic triangles in one layer of the bilayer to the antiferromagnetic triangles in the other layer (and vice versa), as illustrated in Fig. 1e. J_0 competes with the antiferromagnetic intralayer interactions J_{31} and J_{32} , destabilizing the 120° long-range magnetic order in both layers and giving rise to the resonating valence bond ground state¹.

To conclude, we have shown both experimentally and theoretically that $\text{Ca}_{10}\text{Cr}_7\text{O}_{28}$ shows all the signatures expected of a quantum spin liquid, with persistent slow dynamics in the ground state and spinon excitations. This long-sought state arises from a completely new and unexpected frustration mechanism due to a complex Hamiltonian consisting of several different isotropic interactions, including strong ferromagnetic and weaker antiferromagnetic couplings. Furthermore, we find that the spin-liquid phase is highly robust to large changes in the exchange interactions. This contrasts with the accepted models for spin liquids: where for isotropic magnets frustration arises from a single antiferromagnetic interaction (for example, kagome), whereas for anisotropic magnets the anisotropy competes with the interactions (for example, spin ice). Thus quantum spin-liquid behaviour is not restricted to the simple models currently being investigated, but can be more widespread and exist in more complex structures than has previously been assumed.

Methods

Methods, including statements of data availability and any associated accession codes and references, are available in the [online version of this paper](#).

Received 19 November 2015; accepted 14 June 2016;
published online 25 July 2016

References

1. Anderson, P. W. Resonating valence bonds: a new kind of insulator? *Mater. Res. Bull.* **8**, 153–160 (1973).

2. Balents, L. Spin liquids in frustrated magnets. *Nature* **464**, 199–208 (2010).
3. Fennell, T. *et al.* Magnetic coulomb phase in the spin ice $\text{Ho}_2\text{Ti}_2\text{O}_7$. *Science* **326**, 415–417 (2009).
4. Morris, D. J. P. *et al.* Dirac strings and magnetic monopoles in the spin ice $\text{Dy}_2\text{Ti}_2\text{O}_7$. *Science* **326**, 411–414 (2009).
5. Kitaev, A. Anyons in an exactly solved model and beyond. *Ann. Phys.* **321**, 2–111 (2006).
6. Banerjee, A. *et al.* Proximate Kitaev quantum spin liquid behaviour in a honeycomb magnet. *Nature Mater.* **15**, 733–740 (2016).
7. Yan, S., Huse, D. A. & White, S. R. Spin-liquid ground state of the $s=1/2$ kagome Heisenberg antiferromagnet. *Science* **332**, 1173–1176 (2011).
8. Depenbrock, S., McCulloch, I. P. & Schollwöck, U. Nature of the spin-liquid ground state of the $s=1/2$ Heisenberg model on the kagome lattice. *Phys. Rev. Lett.* **109**, 067201 (2012).
9. Wan, Y. & Tchernyshyov, O. Phenomenological Z_2 lattice gauge theory of the spin-liquid state of the kagome Heisenberg antiferromagnet. *Phys. Rev. B* **87**, 104408 (2013).
10. Iqbal, Y., Becca, F., Sorella, S. & Poilblanc, D. Gapless spin-liquid phase in the kagome spin-1/2 Heisenberg antiferromagnet. *Phys. Rev. B* **87**, 060405 (2013).
11. Punk, M., Chowdhury, D. & Sachdev, S. Topological excitations and the dynamic structure factor of spin liquids on the kagome lattice. *Nature Phys.* **10**, 289–293 (2014).
12. Suttner, R., Platt, C., Reuther, J. & Thomale, R. Renormalization group analysis of competing quantum phases in the J_1 – J_2 Heisenberg model on the kagome lattice. *Phys. Rev. B* **89**, 020408 (2014).
13. Han, T.-H. *et al.* Fractionalized excitations in the spin-liquid state of a kagome-lattice antiferromagnet. *Nature* **492**, 406–410 (2012).
14. Fu, M., Imai, T., Han, T.-H. & Lee, Y. S. Evidence for a gapped spin-liquid ground state in a kagome Heisenberg antiferromagnet. *Science* **350**, 655–658 (2015).
15. Gyepesova, D. & Langer, V. $\text{Ca}_{10}(\text{Cr}^{\text{V}}\text{O}_4)_6(\text{Cr}^{\text{VI}}\text{O}_4)_4$, a disordered mixed-valence chromium compound exhibiting inversion twinning. *Acta Cryst.* **C69**, 111–113 (2013).
16. Read, N. & Sachdev, S. Valence-bond and spin-Peierls ground states of low-dimensional quantum antiferromagnets. *Phys. Rev. Lett.* **62**, 1694–1697 (1989).
17. Mydosh, J. A. *Spin Glasses: An Experimental Introduction* (Taylor and Francis, 1993).
18. Mehlawat, K., Sharma, G. & Singh, Y. Fragile magnetic order in the honeycomb lattice iridate Na_2IrO_3 revealed by magnetic impurity doping. *Phys. Rev. B* **92**, 134412 (2015).
19. Cole, K. S. & Cole, R. H. Dispersion and absorption in dielectrics i. Alternating current characteristics. *J. Chem. Phys.* **9**, 341–351 (1941).
20. Yaouanc, A. & Dalmas de Rotier, P. *Muon Spin Rotation, Relaxation and Resonance* (Oxford Univ. Press, 2011).
21. Mendels, P. *et al.* Quantum magnetism in the paratacamite family: towards an ideal kagomé lattice. *Phys. Rev. Lett.* **98**, 077204 (2007).
22. Fåk, B. *et al.* Kapellasite: a kagome quantum spin liquid with competing interactions. *Phys. Rev. Lett.* **109**, 037208 (2012).
23. Clark, L. *et al.* Gapless spin liquid ground state in the $S=1/2$ vanadium oxyfluoride kagome antiferromagnet $[\text{NH}_4]_2[\text{C}_7\text{H}_{14}\text{N}][\text{V}_7\text{O}_6\text{F}_{18}]$. *Phys. Rev. Lett.* **110**, 207208 (2013).
24. Squires, G. L. *Introduction to the Theory of Thermal Neutron Scattering* (Dover, 1996).
25. Carlo, J. P. *et al.* Triplet and in-gap magnetic states in the ground state of the quantum frustrated fcc antiferromagnet Ba_2YMoO_6 . *Phys. Rev. B* **84**, 100404 (2011).
26. de Vries, M. A., McLaughlin, A. C. & Bos, J.-W. G. Valence bond glass on an fcc lattice in the double perovskite Ba_2YMoO_6 . *Phys. Rev. Lett.* **104**, 177202 (2010).
27. Faddeev, L. D. & Takhtajan, L. A. What is the spin of a spin wave? *Phys. Lett. A* **85**, 375–377 (1981).
28. Lake, B., Tennant, D. A., Frost, C. D. & Nagler, S. E. Quantum criticality and universal scaling of a quantum antiferromagnet. *Nature Mater.* **4**, 329–334 (2005).
29. Caux, J.-S. & Hagemans, R. The four-spinon dynamical structure factor of the Heisenberg chain. *J. Stat. Mech.* P12013 (2006).
30. Lake, B. *et al.* Multispinon continua at zero and finite temperature in a near-ideal Heisenberg chain. *Phys. Rev. Lett.* **111**, 137205 (2013).
31. Mourigal, M. *et al.* Fractional spinon excitations in the quantum Heisenberg antiferromagnetic chain. *Nature Phys.* **9**, 435–441 (2013).
32. Balz, C. *et al.* Quantum spin chain as a potential realization of the Nersisyan–Tselik model. *Phys. Rev. B* **90**, 060409 (2014).
33. Liang, S., Doucot, B. & Anderson, P. W. Some new variational resonating-valence-bond-type wave functions for the spin-1/2 antiferromagnetic Heisenberg model on a square lattice. *Phys. Rev. Lett.* **61**, 365–368 (1988).
34. Read, N. & Chakraborty, B. Statistics of the excitations of the resonating-valence-bond state. *Phys. Rev. B* **40**, 7133–7140 (1989).
35. Read, N. & Sachdev, S. Large- N expansion for frustrated quantum antiferromagnets. *Phys. Rev. Lett.* **66**, 1773–1776 (1991).
36. Wen, X. G. Mean-field theory of spin-liquid states with finite energy gap and topological orders. *Phys. Rev. B* **44**, 2664–2672 (1991).
37. Wen, X.-G. Quantum orders and symmetric spin liquids. *Phys. Rev. B* **65**, 165113 (2002).
38. Coldea, R. *et al.* Direct measurement of the spin Hamiltonian and observation of condensation of magnons in the 2D frustrated quantum magnet Cs_2CuCl_4 . *Phys. Rev. Lett.* **88**, 137203 (2002).
39. Ross, K. A., Savary, L., Gaulin, B. D. & Balents, L. Quantum excitations in quantum spin ice. *Phys. Rev. X* **1**, 021002 (2011).
40. Toth, S. & Lake, B. Linear spin wave theory for single-Q incommensurate magnetic structures. *J. Phys. Condens. Matter* **27**, 166002 (2015).
41. Reuther, J. & Wölfle, P. J_1 – J_2 frustrated two-dimensional Heisenberg model: random phase approximation and functional renormalization group. *Phys. Rev. B* **81**, 144410 (2010).
42. Reuther, J. & Thomale, R. Functional renormalization group for the anisotropic triangular antiferromagnet. *Phys. Rev. B* **83**, 024402 (2011).
43. Reuther, J., Thomale, R. & Rachel, S. Spiral order in the honeycomb iridate Li_2IrO_3 . *Phys. Rev. B* **90**, 100405 (2014).
44. Chernyshev, A. L. & Zhitomirsky, M. E. Spin waves in a triangular lattice antiferromagnet: decays, spectrum renormalization, and singularities. *Phys. Rev. B* **79**, 144416 (2009).
45. Frontzek, M. *et al.* Magnetic excitations in the geometric frustrated multiferroic CuCrO_2 . *Phys. Rev. B* **84**, 094448 (2011).
46. Kubo, R. & Toyabe, T. *Magnetic Resonance and Relaxation* (North-Holland, 1967).

Acknowledgements

We thank S. Toth for his help with the SpinW program and E. J. Bergholtz for helpful discussions. We acknowledge the Helmholtz Gemeinschaft for funding via the Helmholtz Virtual Institute (Project No. HVI-521) and DFG through Research Training Group GRK 1621 and SFB 1143. We also acknowledge the support of the HLD-HZDR, a member of the European Magnetic Field Laboratory (EMFL). This work used facilities supported in part by the National Science Foundation under Agreement No. DMR-1508249. J.R. was supported by the Freie Universität Berlin, within the Excellence Initiative of the German Research Foundation.

Author contributions

C.B. performed or participated in all measurements, and analysed the data with help from the other authors. B.L. directed the project, participated in most measurements, and wrote the manuscript with contributions from all authors. J.R. carried out the PFFRG calculations and provided theoretical insight. Y.S. introduced the compound and made the powder, while the crystals were grown by Y.S. and A.T.M.N.I.; H.R. carried out the specific heat measurements; R.S. and T.H. performed the AC susceptibility measurements and helped with the analysis; C.B. and H.L. helped with the μSR measurements and with their analysis; E.M.W., J.A.R.-R., T.G. and G.G.S. supported the INS measurements.

Additional information

Supplementary information is available in the [online version of the paper](#). Reprints and permissions information is available online at www.nature.com/reprints. Correspondence and requests for materials should be addressed to C.B.

Competing financial interests

The authors declare no competing financial interests.

Methods

Sample preparation. The samples were prepared at Crystal Lab, Helmholtz Zentrum Berlin für Materialien und Energie, Germany. The powder samples were made from high-purity powders of CaCO_3 (Alfa Aesar, 99.95%) and Cr_2O_3 (Alfa Aesar, 99.97%). The starting materials were mixed thoroughly in a 3:1 ratio and calcined in air at 1,000 °C for 24 h. The single crystal was grown by the travelling-solvent floating-zone technique using an optical image furnace (Crystal Systems, Japan). A cylindrical feed rod was prepared from the powder, which was pressed hydrostatically up to 3,000 bar in a cold isostatic press and sintered in air at 1,010 °C for 12 h, followed by rapid quenching to room temperature. A solvent with the composition 71.5 mol% CaCO_3 and 28.5 mol% Cr_2O_3 was prepared in the same way, approximately 0.5 g of which was attached to the tip of the feed rod to start the growth. A stable growth was achieved under an oxygen atmosphere of 2 bar with a growth rate of 1 mm h⁻¹. Two single-crystalline pieces, each about 15 mm in length and 6 mm in diameter, were obtained by this process.

Measurements. The specific heat was measured down to 300 mK on a 0.91 mg single crystal using a relaxation technique at the Laboratory for Magnetic Measurements, Helmholtz Zentrum Berlin für Materialien und Energie, Germany. The heat capacity is corrected for the phonon contribution by fitting a Debye-like contribution ($C_p = \alpha T^3$) to the data points above 20 K and subtracting the fitted curve from the raw data. The a.c. susceptibility was measured down to 50 mK on a 49 mg single crystal using a compensated coil pair system at the Dresden High Magnetic Field Laboratory, Helmholtz Zentrum Dresden Rossendorf, Germany. The μSR measurements took place on the LTF and GPS spectrometers at the Laboratory for Muon Spin Spectroscopy, Paul Scherrer Institute, Switzerland. For the LTF measurement, 200 mg of powder was spread on a Ag backing plate and mixed with a small drop of alcohol-diluted GE Varnish for better thermal conductivity. The measurement on GPS was performed on a 300 mg powder sample in a thin Ag foil packet. Zero- and longitudinal-field measurements were performed for temperatures from 19 mK to 210 K. The data were analysed using the musrfit software package⁴⁷. The powder inelastic neutron scattering experiment was performed on the time-of-flight spectrometer TOFTOF at the Heinz Maier Leibnitz Zentrum, Munich, Germany at a temperature of 430 mK using 8.14 g of powder. An incident energy of 3.27 meV was used, giving a resolution of 0.08 meV. The data were binned into steps of 0.02 Å and 0.02 meV. The single-crystal inelastic neutron scattering experiments were performed on the triple-axis spectrometers IN14 with the flat cone option at the Institut Laue-Langevin, Grenoble, France and MACS II at the NIST Center for Neutron Research, Gaithersburg, USA. Additional data were taken on the indirect time-of-flight spectrometer OSIRIS at the ISIS facility, Didcot, UK. At IN14, two single crystals with masses of 0.97 g and 0.74 g were measured, with scattering planes ($h0l$) and ($hk0$), respectively. The measurements took place at a temperature of 1.6 K and the final neutron energy was fixed to 4.06 meV, giving a resolution of 0.12 meV. The data was binned into steps of 0.0085 along $[h, h, 0]$, 0.013 along $[h, -h, 0]$ and 0.06 along $[0, 0, l]$, and the binned slices were then smoothed by a weighted average over 1.5 bins. For the MACS II experiment the two single crystals (total mass 1.71 g) were co-aligned with the ($hk0$) plane horizontal and were measured at 90 mK. The final energy was

fixed at 3.7 meV, giving a resolution of 0.33 meV. The data was binned into steps of 0.035 along $[h, h, 0]$ and 0.06 along $[h, -h, 0]$. The same specimen was also used on OSIRIS at a temperature of 220 mK and a energy resolution of 0.025 meV. The data was binned into steps of 0.05 r.l.u. and 0.05 meV, and smoothed with a hat function of width 2 bins.

Pseudofermion functional renormalization group calculations. In the PFFRG approach, the spin Hamiltonian is first rewritten in terms of Abrikosov pseudofermions as

$$S_i^\mu = \frac{1}{2} \sum_{\alpha\beta} f_{i\alpha}^\dagger \sigma_{\alpha\beta}^\mu f_{i\beta} \quad (2)$$

with $\alpha, \beta = \uparrow, \downarrow$. Here $f_{i\alpha}^{(\dagger)}$ denotes a pseudofermion annihilation (creation) operator of spin α at site i , and $\sigma_{\alpha\beta}^\mu$ are the Pauli matrices ($\mu = x, y, z$). The resulting quartic Hamiltonian is then treated via the functional renormalization group approach⁴¹. This method formulates equations for the renormalization group flow of all fermionic m -particle vertices as a function of an infrared frequency cutoff Λ . To obtain a closed set of equations, three-particle vertices are neglected, except for those which can be written as a self-energy insertion in the two-particle vertex. This truncation scheme yields self-consistent diagrammatic resummations in different interaction channels and in infinite order in the exchange couplings. The central outcome of the PFFRG is the momentum-resolved d.c. magnetic susceptibility, which directly follows from the fermionic two-particle vertex. A magnetically ordered ground state is signalled by a pronounced cusp or a kink during the flow of the susceptibility, while a smooth flow indicates non-magnetic behaviour. For more details on the method, see the Supplementary Methods or the recent reviews^{48,49}.

Data availability. Raw μSR data were measured using the LTF and GPS spectrometers at the Laboratory for Muon Spin Spectroscopy, Paul Scherrer Institute, Switzerland. Raw powder inelastic neutron scattering data were measured on the time-of-flight spectrometer TOFTOF at the Heinz Maier Leibnitz Zentrum, Munich, Germany. Single-crystal inelastic neutron scattering data were measured on the triple-axis spectrometers IN14 with the flat cone option at the Institut Laue-Langevin, Grenoble, France and MACS II at the NIST Center for Neutron Research, Gaithersburg, USA. Additional data were taken on the indirect time-of-flight spectrometer OSIRIS at the ISIS facility, Didcot, UK. All other raw and derived data used to support the findings of this study are available from the authors on request.

References

- Suter, A. & Wojek, B. M. Musrfit: a free platform-independent framework for μsr data analysis. *Phys. Proc.* **30**, 69–73 (2012).
- Metzner, W., Salmhofer, M., Honerkamp, C., Meden, V. & Schönhammer, K. Functional renormalization group approach to correlated fermion systems. *Rev. Mod. Phys.* **84**, 299–352 (2012).
- Platt, C., Hanke, W. & Thomale, R. Functional renormalization group for multi-orbital fermi surface instabilities. *Adv. Phys.* **62**, 453–562 (2013).